Spherical Navigator Echoes for Full 3D Rigid Body Motion Measurement in MRI

Edward Brian Welch,[1,3] Armando Manduca,[2,3] Roger C. Grimm,[1] Heidi A. Ward,[1,3] and Clifford R. Jack, Jr.[1,3*]

We developed a 3D spherical navigator (SNAV) echo technique that can measure rigid body motion in all six degrees of freedom simultaneously by sampling a spherical shell in *k*-space. 3D rotations of an imaged object simply rotate the data on this shell and can be detected by registration of *k*-space magnitude values. 3D translations add phase shifts to the data on the shell and can be detected with a weighted least-squares fit to the phase differences at corresponding points. MRI pulse sequences were developed to study *k*-space sampling strategies on such a shell. Data collected with a computer-controlled motion phantom with known rotational and translational motions were used to evaluate the technique. The accuracy and precision of the technique depend on the sampling density. Roughly 2000 sample points were necessary for accurate detection to within the error limits of the motion phantom when using a prototype time-intensive sampling method. This number of samples can be captured in an approximately 27-ms double excitation SNAV pulse sequence with a 3D helical spiral trajectory. Preliminary results with the helical SNAV are encouraging and indicate that accurate motion measurement suitable for retrospective or prospective correction should be feasible with SNAV echoes. Magn Reson Med 47:32–41, 2002.

Key words: motion correction; rotation; navigator echo; sphere

Patient motion remains a significant problem in many MRI applications, including fMRI, cardiac and abdominal imaging, and conventional long TR acquisitions. Many techniques are available to reduce or to compensate for bulk motion effects, such as physiologic gating (1), phase-encode reordering (2–4), fiducial markers (5), fast acquisitions (6–7), image volume registration (8,9), or alternative data acquisitions strategies such as projection reconstruction (10–12), spiral (11), and PROPELLER (13). Navigator echoes are used to measure motion in one or more degrees of freedom; the motion is then compensated for either retrospectively (14) or prospectively (15). An orbital navigator (ONAV) echo (16) captures data in a circle in some plane of *k*-space, centered at the origin. This data can be used to detect rotational and translational motion in this plane, and to correct for this motion either prospectively or retrospectively. However, multiple orthogonal ONAVs are required for general 3D motion determination, and the accuracy of a given ONAV is adversely affected by motion out of its plane (17–20). We have developed a 3D spherical navigator (SNAV) echo technique that can measure rigid body motion with high accuracy in all six degrees of freedom simultaneously by sampling a spherical shell of *k*-space centered at the origin. This sampling can be performed in tens of milliseconds, making the technique potentially useful for motion correction in a variety of MRI applications.

THEORY

The SNAV generalizes the ONAV concept by sampling data in a spherical shell of *k*-space centered at the origin. As described in Ref. 19, 3D rotations of an imaged object rotate the data on this shell, and can be detected by registration of the magnitude values before and after the motion. 3D translations add phase shifts to the data on the shell and can be detected after the rotational corrections are performed. If one ignores the effects of tissue entering or leaving the field of view (FOV), *k*-space data never enters or leaves the spherical shell in the case of rigid body motion. The relationship between a baseline position signal S measured at the original location (k_x, k_y, k_z) and a later signal S' measured in a new rotated coordinate system (k_x', k_y', k_z') with translation $(\Delta x, \Delta y, \Delta z)$ is expressed in Eq. [1]. The same relation expressed in spherical coordinates is shown in Eq. [2]. Notice that the *k*-space radius, k_ρ, is unchanged in the new rotated coordinate frame because the signal is collected on a spherical shell.

$$S'(k_x',k_y',k_z') = S(k_x,k_y,k_z)e^{i2\pi(\Delta x k_x+\Delta y k_y+\Delta z k_z)} \quad [1]$$

$$S'(k_\rho,\theta',\phi') = S(k_\rho,\theta,\phi)e^{i2\pi k_\rho(\Delta x\cos\theta\sin\phi+\Delta y\sin\theta\sin\phi+\Delta z\cos\phi)} \quad [2]$$

Rotations of an object in the spatial domain correspond to rotations in *k*-space, which in this case means that points simply rotate on the spherical surface and their magnitude values do not change. Off-center rotations are mathematically equivalent to an on-center rotation plus an apparent translation of the coordinate frame, and can be treated in this manner, as is done for ONAVs. Translations in image space do not affect the *k*-space magnitude, and add only the phase shifts shown.

Determination of Rotation

The magnitude data on a spherical surface in *k*-space at an appropriate radius has features of high and low values, depending on the object being imaged. This "intensity texture" rotates (Fig. 1) with arbitrary 3D rotations, so the patterns before and after a rotation can be matched up, and the rotation parameters that yield the best match deduced.

[1]MRI Research Lab, Department of Diagnostic Radiology, Mayo Clinic, Rochester, Minnesota.

[2]Biomathematics Resource, Mayo Clinic, Rochester, Minnesota.

[3]Mayo Graduate School, Mayo Clinic, Rochester, Minnesota.

Grant sponsor: NIH; Grant numbers: CA73691; AG19142.

*Correspondence to: Clifford R. Jack, Jr., M.D., Department of Radiology, Mayo Clinic, 200 First Street SW, Rochester, MN 55905. E-mail: jack.clifford@mayo.edu

Received 22 May 2001; revised 13 July 2001; accepted 22 July 2001.

DOI 10.1002/mrm.10012

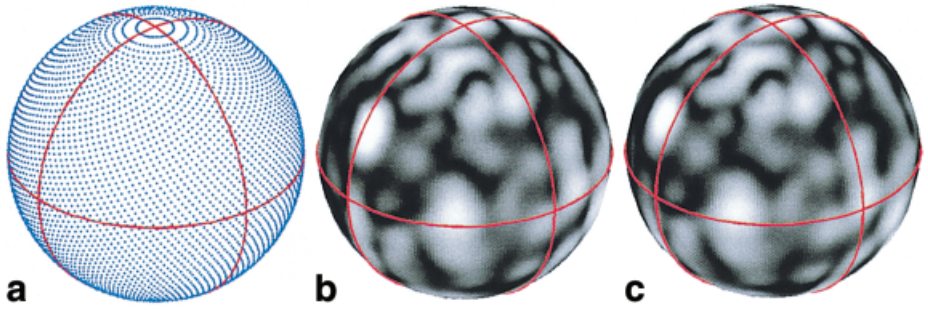

FIG. 1. Signal amplitude maps of the *k*-space magnitude of the skull phantom at $k_\rho = 0.625$ cm^{-1} ($15\Delta k$) (**b**) before and (**c**) after a 12° relative rotation by the computer-controlled motion phantom about the k_z axis (the pole-to-pole axis). **a:** The dense sampling strategy comprised of 256 ONAVs sampling equally spaced lines of latitude is displayed with only every 10th sample of 62464 samples plotted. The magnitude features are stable and rotate as expected. Great circles are drawn as an aid to visualize rotation, but also represent the *k*-space trajectory of three orthogonal ONAV echoes. Rotation may confound the ONAV technique because magnitude features will rotate out-of-plane for at least two of the orthogonal ONAVs for any given rotation.

This is simply a registration problem, analogous to rotating the earth's surface in an arbitrary way and deducing the rotation parameters by "lining up" the mountain ranges and valleys. This registration process is straightforward provided that there are sufficient features on the spherical surface and that it is sampled densely enough. Registration is performed here by minimizing a sum of squared differences cost function that measures the degree of mismatch between the magnitude values of an original static baseline SNAV data set and a second later SNAV data set as trial rotations are applied to the latter.

There are many conventions for expressing 3D rotations. We chose to apply rotation angles θ_x, θ_y, θ_z about the rotated *x*, *y*, *z* axes in that order, but any other convention (including a quaternion representation) would work equally well. The convention used here is represented by

$$\begin{bmatrix} k_x \\ k_y \\ k_z \end{bmatrix} = \mathbf{M} \begin{bmatrix} k'_x \\ k'_y \\ k'_z \end{bmatrix} \text{ with rotation matrix } \mathbf{M}$$

$$= \begin{bmatrix} c_y c_z & s_x s_y c_z - c_x s_z & c_x s_y c_z + s_x s_z \\ c_y s_z & s_x s_y s_z + c_x c_z & c_x s_y s_z - s_x c_z \\ -s_y & s_x c_y & c_x c_y \end{bmatrix} \quad [3]$$

where $c_x = \cos(\theta_x)$, $s_y = \sin(\theta_y)$, etc. For each sample point of the second SNAV, its rotated position was found, and the corresponding magnitude value of the baseline data set at that point's position was interpolated from nearby points. The 3D coordinates of the data were converted to a latitude and longitude coordinate system in order to use an efficient 2D Delaunay triangulation algorithm suitable for interpolation of nonuniformly-spaced data. The samples of the regularly spaced interpolated 2D grids were then registered using bilinear interpolation. The squared difference between the interpolated magnitude value from the baseline data and the measured value from the match data was calculated, and this difference was summed over all sample points. Downhill simplex minimization (21) was used to optimize this cost function. All three rotation angles were solved for simultaneously by the algorithm, which typically required 20–50 iterations to converge.

Determination of Translation

Translational motion does not alter magnitude values on the spherical shell, but it does alter phase values. At each point in 3D *k*-space, a translation of (Δx, Δy, Δz) causes a phase change $\Delta\Phi$ according to Eq. [4]. If the shell is sampled with *N* points, then each point yields an equation of this form, giving a system of *N* equations in three unknowns. The calculation of translation is thus highly overdetermined and is expected to be quite robust.

$$\Delta\Phi = 2\pi[\Delta x k_x + \Delta y k_y + \Delta z k_z] \quad [4]$$

The raw phase differences may exceed the range $\pm\pi$. Values outside the range may be folded back into this range by adding or subtracting 2π. This is valid as long as the translations are small enough to avoid true phase wraps (translations smaller than $0.5/k_\rho$). Translations larger than $0.5/k_\rho$ will cause absolute phase changes greater than π (outside the range of $\pm\pi$), which would require the use of phase unwrapping algorithms before processing.

After an SNAV is registered to a baseline SNAV by any necessary rotation(s), interpolated phase values are calculated for the rotated SNAV at the original sample positions. The phase differences between the two SNAVs are then inserted into a weighted least-squares inversion to find the (Δx, Δy, Δz) translations, similar to how (Δx, Δy) translations are detected with ONAV echoes (19,20). Equations [5]–[8] describe this weighted least-squares inversion calculation performed on the *k*-space phase differences. The 3×1 column vector **x** contains the unknown motions. The elements of the $N \times 1$ column vector **b** are the phase differences. The rows of the $N \times 3$ matrix **A** contain the (k_x, k_y, k_z) position of each sampled point in *k*-space. The $N \times N$ diagonal weighting matrix **W** added in Eq. [6] contains each sample's magnitude as its weight to account for higher noise in the phase at low magnitude positions in *k*-space. After calculating the inverse of the 3×3 matrix **Q** defined in Eq. [7], one can find the best least-squares fit (Δx, Δy, Δz) translations in **x** using Eq. [8].

$$\mathbf{Ax} = \mathbf{b} \quad [5]$$

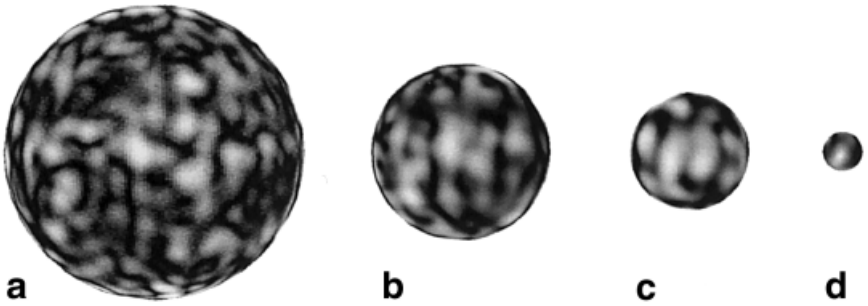

FIG. 2. Signal amplitude maps of the *k*-space magnitude of the skull phantom at four different radii in *k*-space. The displayed radii are (**a**) 25Δ*k*, (**b**) 15Δ*k*, (**c**) 10Δ*k*, and (**d**) 5Δ*k* (Δ*k* = 0.0417 cm^{-1}). The displayed gray scale intensity has been individually histogram equalized for each of the four images in order to compare feature detail. The magnitude features increase in detail as the radius increases, but SNR decreases.

$$(\mathbf{A}^T\mathbf{W}\mathbf{A})\mathbf{x} = \mathbf{A}^T\mathbf{W}\mathbf{b} \quad [6]$$

$$\mathbf{Q} = \mathbf{A}^T\mathbf{W}\mathbf{A} \quad [7]$$

$$\mathbf{x} = \mathbf{Q}^{-1}\mathbf{A}^T\mathbf{W}\mathbf{b} \quad [8]$$

METHODS

Sampling the *k*-Space Sphere

Two schemes are presented here for sampling the *k*-space sphere. The first is a dense sampling strategy useful for validation studies and is comprised of many parallel ONAV echoes, as represented in Fig. 1a. The second is a double excitation with two spherical helix echoes that begin at the equator and move toward one or the other pole of the sphere, as described below. Experiments were performed with the two acquisition schemes to confirm the theory of the movement of data magnitude and changes in data phase on a *k*-space spherical shell undergoing rotation and translation. The densely sampled data were also used to study the effect of sampling density on rotation detection ability.

The magnitude features in *k*-space depend on the radius of the spherical shell. The theoretical rotation and translation detection algorithms described above should work well if the spherical shell has sufficient features and is sampled densely enough at high enough signal-to-noise ratio (SNR). If the radius of the shell is too small, fewer features are present; conversely, if the radius is too large, the SNR is lower. This relationship between *k*-space radius and magnitude features is illustrated in Fig. 2. Figures 2b and 1b and c were collected at the same *k*-space radius of 0.625 cm^{-1} (15Δ*k*); however, Fig. 2b is displayed at a different viewpoint. For the motion experiments presented, the radius of the implemented trajectories for sampling the *k*-space sphere were chosen with *k*-space magnitude feature density, SNR, and slew rate limits in mind. The design of the implemented trajectory and the associated trade-offs are described later.

Computer-Controlled Motion Phantom

To validate the SNAV it was necessary to have a means of inducing precise known motions in an imaged object. In the experiments described below, a computer-controlled motion phantom was used that is capable of precise rotations and translations in multiple planes (19). Computer-controlled stepper motors in the phantom were able to create sagittal rotation, axial rotation, and *z* translation. The imaged object was a gel-filled model of a human skull generated by a CT modeler at 75% scale (13 cm × 9 cm × 9 cm). The reduced scale was necessary to reduce the moment of inertia and improve the accuracy of applied axial rotations. Glass rods within the skull served as fiducial markers. Previous calibration studies found the phantom to be accurate to ±0.13° for sagittal rotations, ±0.5° for axial rotations, and ±0.2 mm for translations (19).

Dense Sphere Sampling

In the initial pilot stage of this work, we examined the accuracy and precision of rotation detection only. Translation detection was addressed in later experiments. Motion phantom rotations of +5.98°, +3.16°, –3.16°, and –5.98° (the motion phantom performs rotations in quantized steps that are not an even multiple of degrees) were performed in the axial and sagittal directions separately. At each phantom position, spherical data and ONAV data were collected, analyzed, and compared with the intended rotation. With the dense sphere sampling strategy, 244 complex points were acquired in a circular trajectory parallel to the k_x–k_y plane and centered about the k_z axis, as shown in Fig. 1a. This was repeated 256 times, with the position along the k_z axis incremented uniformly from a starting point of $k_z = +k_\rho$ to $k_z = -k_\rho$, where k_ρ is the radius of a sphere centered at the origin. The radius of each of the 256 circular navigator echoes was altered so the sample points describe a spherical shell in *k*-space, with the 62464 total points forming a grid in latitude and longitude. This sampling strategy is not optimal since the points are not uniformly distributed—near the equator, latitude (ϕ) is sampled roughly twice as finely as longitude (θ), and points near the poles are too close together in θ and too far apart in ϕ. Also, the acquisition time is far too long to be practical for actual in vivo motion correction applications. However, this strategy was ideal for acquiring very dense sampling of the spherical shell for initial studies. Sampling at lower density was simulated by simply decimating the data to a smaller number of rows and columns; e.g., using only every fourth row and eighth column gives a data set of 1952 points.

Double Excitation Spherical Helix Sampling

Ideally, one would like to sample a sufficient number of points on the spherical shell for accurate motion determination as quickly as possible and cover the sphere as uniformly as possible. Our next objective was to design an SNAV acquisition scheme that accurately encoded mo-

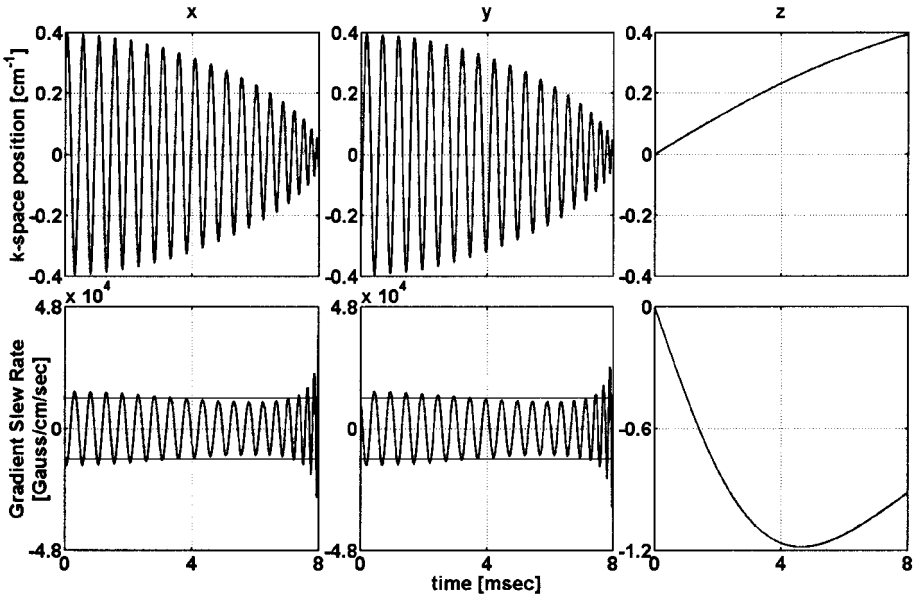

FIG. 3. Plots of the *k*-space trajectory (top) and associated gradient slew rates (bottom) for sampling an entire hemisphere with radius k_ρ = 0.396 cm^{-1} (9.5Δk). The maximum slew rate of 12000 Gauss/cm/s (horizontal lines) is exceeded in the k_x and k_y trajectories slightly near the equator and to a greater extent near the pole.

tion, yet could be executed rapidly enough to be clinically usable. This required consideration of several trade-offs. Based on the dense sampling results described earlier, we needed at least 2000 sample points. The following objectives were also considered: 1) minimize sampling time in order to minimize T_2^* decay effects; 2) maximize the number of "cross thread" helical turns to increase sensitivity to "cross thread" rotation, without exceeding gradient slew rate limits; 3) maximize *k*-space sampling radius (k_ρ) to increase feature density, without exceeding gradient slew rate limits; and 4) acquire data in a manner that minimized sensitivity to linear B_o field gradients in the k_z direction. We arrived at a double spherical helical sampling strategy. Equations describing an approximately uniform distribution of points on a sphere following a spherical helical trajectory have been described elsewhere (22) and are stated in Eqs. [9]–[11] in the form of discrete (x, y, z) coordinates on the unit sphere. The variable N is the total number of sample points, and Eq. [9] shows that the z-coordinate of the trajectory is linear. The x and y coordinates are calculated based on the z position of the nth sample in Eqs. [10] and [11].

$$z[n] = \frac{2n - N - 1}{N} \qquad [9]$$

$$x[n] = \cos(\sqrt{N\pi}\,\sin^{-1}z[n])\,\sqrt{1 - z^2[n]} \qquad [10]$$

$$y[n] = \sin(\sqrt{N\pi}\,\sin^{-1}z[n])\,\sqrt{1 - z^2[n]} \qquad [11]$$

In MRI, sampling a *k*-space sphere with such a spherical helix trajectory will have high slew rates on the k_x and k_y axes. This problem is illustrated in Fig. 3, in which the *k*-space trajectory and associated gradient slew rates are plotted for a spherical helix trajectory sampling a hemisphere with radius k_ρ = 0.396 cm^{-1} (9.5Δk). The slew rate limit for the Echospeed gradient set on the GE Signa full-body imager used in these experiments is 12000 Gauss/cm/s and is exceeded by the *k*-space trajectory required to completely sam-

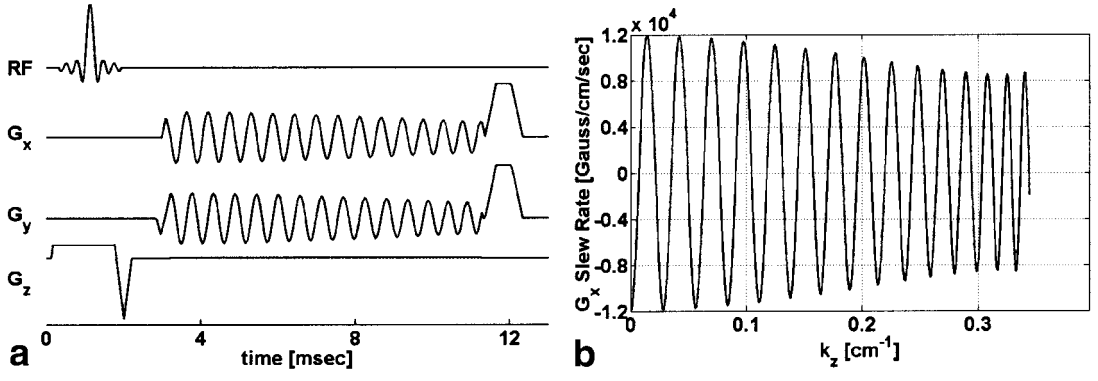

FIG. 4. (**a**) RF and gradient waveforms and (**b**) slew rate of the G_x gradient for the implemented hemispheric trajectory; 1008 points on the spherical surface are sampled in 8 ms. By beginning at the equator and traveling towards the pole, the implemented trajectory is always within gradient slew rate limits and is still able to sample 85% of the hemisphere's area at k_ρ = 0.396 cm^{-1} (9.5Δk).

Table 1
Dense Sphere Sampling Rotation Detection Versus Orthogonal ONAV Results

	Axial rotation (°)				Sagittal rotation (°)			
Intended motion	−5.98	−3.16	3.16	5.98	−5.98	−3.16	3.16	5.98
Sphere detection	−5.43	−2.49	3.18	5.81	−6.02	−3.15	3.30	6.15
ONAV detection	−5.27	−2.46	3.16	5.98	−5.98	−3.51	3.16	5.63

ple the hemisphere. Slew rates are highest as the trajectory spirals tightly near the pole, and therefore it is possible to stay within slew rate limitations by stopping the spherical helix trajectory at a maximum k_z that is less than k_ρ. This will leave a small area at the pole of the sphere unsampled, with this fraction being directly proportional to the maximum k_z of the spherical helix trajectory, as stated in Eq. [12]. To accommodate the missing portions of the sphere, the registration algorithm was altered to include an input parameter to specify the number of lines of latitude to ignore near the poles of the sphere. This number was chosen to be high enough so that the unsampled portions of the sphere would not interfere with the registration for the expected range of rotation. Figure 4 shows the RF and gradient waveforms and the corresponding slew rate of the G_x gradient for the implemented SNAV echo in which 1008 samples are collected in an 8-ms readout window.

$$\text{Area}_{\text{Sampled}} = \text{Area}_{\text{Total}}\left(\frac{k_{z\max}}{k_\rho}\right) \qquad [12]$$

It is possible to sample 85% of the k-space hemisphere's area in the 8-ms readout time and still satisfy slew rate limits. The slew rate of the G_x gradient remains below the 12000 Gauss/cm/s limit (Fig. 4b). In addition to satisfying slew rate limits, a clinically feasible SNAV implementation will have to observe dB/dt limits that depend on coil geometry. For the head coil and full volume excitation used for the experiments presented here, dB/dt limits are satisfied by the implemented SNAV design. This flexible SNAV design makes it possible to sample data at even larger k-space radii by sampling a smaller proportion of the k-space hemisphere's area. Increasing the readout time will reduce slew rates and allow one to sample a sphere with larger radius as well, although eventually T_2^* decay becomes a problem. To avoid T_2^* decay effects, the duration of the SNAV readout was limited to 8 ms, making it possible to sample 1008 points on the spherical surface with a receiver bandwidth of 125 kHz.

The other hemisphere of the k-space spherical shell is sampled by a second SNAV pulse. In addition to covering more area of the sphere, the second pulse is necessary to avoid being vulnerable to additional phase errors due to the motion itself. Motion of an imaged object may introduce B_o inhomogeneities, which were not present during baseline shimming. The uncompensated B_o field inhomogeneity produces a phase ramp with time in the match navigator echo relative to the premotion reference navigator (20). If the navigator echo trajectory has a component that is nearly linear with time (in this case k_z), the additional phase ramp will result in an apparent translation from the weighted least-squares calculations. The double SNAV pulse avoids this bias by sampling the sphere such that the k_z trajectory is orthogonal to a trajectory that is linear-with-time.

To test the accuracy of motion detection by the double excitation spherical helix SNAV echo, the computer-controlled motion phantom was imaged separately at a baseline position and at translations of −5, −3, +3, and +5 mm, and at rotated positions of +4.92°, +3.16°, −3.16°, and −4.92°. Motions of these amplitudes are frequently encountered in clinical fMRI studies (23–25). The orientation of the collected SNAV and ONAVs was rotated so that the unidirectional motion of the computer-controlled motion phantom appeared as a motion along the k_z axis ("cross thread" orientation) or perpendicular to the k_z axis ("along thread" orientation). At each phantom position, 24 repetitions of the SNAV and ONAV acquisitions were collected in order to estimate the reproducibility of motion detection.

RESULTS

Dense Sphere Sampling

Displays of the magnitude of the acquired data show the expected rotation of features. Figure 1 depicts two rotated positions of the phantom for rotations about the k_z axis at a k-space radius of $15\Delta k$ (0.625 cm^{-1}). The rotation detection results for the full grid of 62464 points are shown in Table 1 for both axial and sagittal rotations of the phantom, along with the result from the corresponding in-plane ONAV. The dense spherically sampled results match well with the ONAV results and the intended rotations (i.e., those programmed into the phantom stepper motors), except for the negative axial cases, for which both the spherical and ONAV results (as well as visual inspection) indicate that the actual rotation was somewhat less than the intended value. The rotations reported by the spherical technique about the other two (nonrotated) axes were usually within ±0.1° and always within ±0.2° of the expected value of zero.

Given that the SNAV approach works well with very dense sampling, the next key question was, how many points are sufficient for precise rotational determination? Sampling at lower density was simulated by decimating the data as described above. The results in Fig. 5 show how the performance of the algorithm degrades as the number of points decreases. The algorithm performed very reliably with as few as 1952 points, and began to degrade significantly only when the number of points fell below 1000–1200. Using only 1952 points, the accuracy of the algorithm for these data sets was within ± 0.1° for all axes. However, this distribution of sample points is not optimal. Results should improve and fewer points should be required with a more uniform sampling strategy, such as the spherical helix. The number of samples necessary for ac-

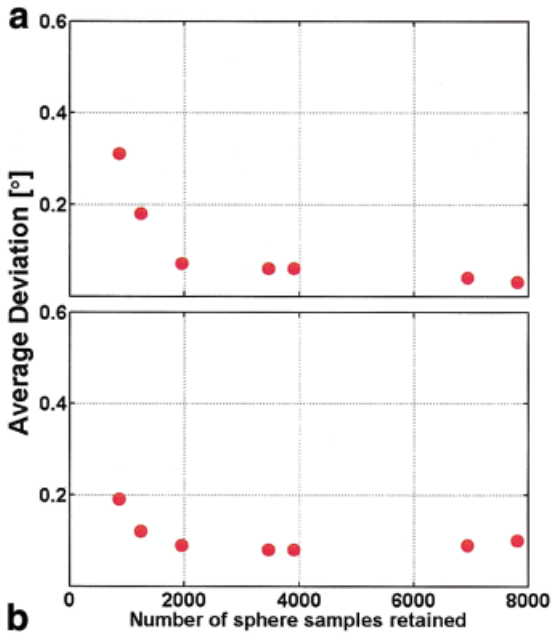

FIG. 5. Effects of reducing sampling density on detected rotation. Average absolute deviation from full sample grid results was calculated for results along the (**a**) axes of motion and for the rotations determined for the (**b**) other two (nonrotated) axes. The differences in the results for both axial and sagittal rotations detected using smaller numbers of sample points were compared to the results for the full 62464 points. The algorithm consistently found values less than ±0.1° on average, with as few as 1250 points.

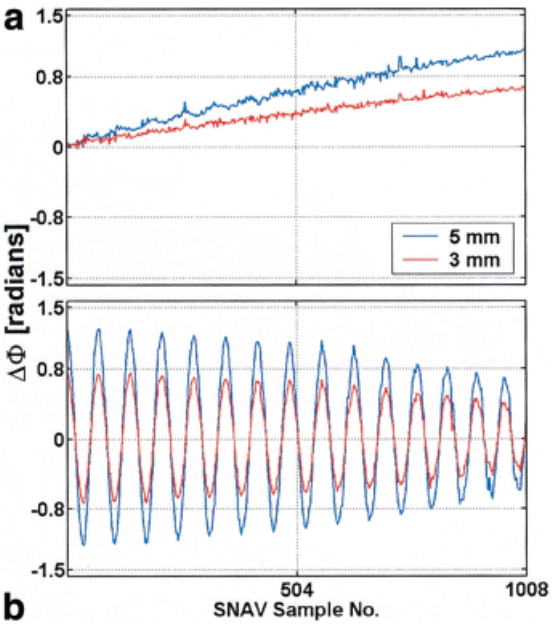

FIG. 7. Phase difference plots caused by translations of 5 mm and 3 mm in the (**a**) "cross thread" (*z*) direction and the (**b**) "along thread" (*x*) direction. Because the translation was entirely along one of the magnet's principal axes, the plots resemble components of the SNAV trajectory. The shapes and amplitudes are correct for k_ρ = 0.396 cm^{-1} (9.5Δ*k*).

curate detection is heavily dependent on the *k*-space magnitude feature detail, which depends on the imaged object and also varies across different radii of *k*-space. The choice of radius and sampling density should thus be application dependent.

Double Excitation Spherical Helix Sampling

Two hemispheric echoes were collected as depicted in Fig. 6a, which also displays the SNAV magnitude for the phantom at two rotated positions (Fig. 6b and c). The features are not as detailed as in Fig. 1 because the SNAV data is collected at a smaller *k*-space radius. The unsampled portions of *k*-space appear as black polar "ice caps" which represent only 15% of the sphere's area. Sample phase differences between SNAVs caused by translation are plotted in Fig. 7 for both the "cross thread" (Fig. 7a) and "along thread" (Fig. 7b) echo orientation. Only the phase difference for the first echo of the hemispheric pair is plotted. Because the translations were entirely along one of the magnet's principal axes, the plots resemble components of the SNAV trajectory itself. The shapes and amplitudes are correct for k_ρ = 0.396 cm^{-1} (9.5Δ*k*). If a translation occurred along an axis other than one of the principal axes, the phase difference plot would be a weighted sum of the k_x, k_y, and k_z trajectories. The trajectories form an orthogonal basis, and translation along any arbitrary axis can be determined with the weighted least-squares inversion.

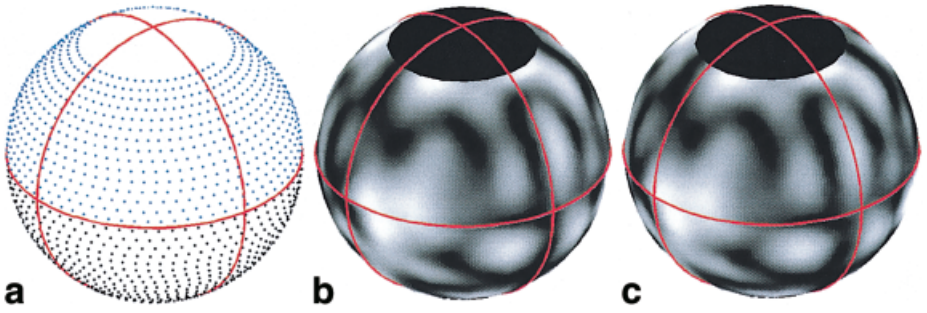

FIG. 6. Signal amplitude maps of *k*-space magnitude at k_ρ = 0.396 cm^{-1} (9.5Δ*k*) (**b**) before and (**c**) after a 10° rotation by the computer-controlled motion phantom about the k_z axis (axial rotation). **a:** The SNAV sampling scheme is displayed with the first SNAV samples above the equator and the second SNAV samples below the equator. The dual hemisphere sampling is performed to make the combined k_z trajectory orthogonal with any possible motion-induced linear-with-time phase accrual. The texture maps represent 2016 samples. The unsampled region near the pole appears black and represents only 15% of the hemisphere's area.

Table 2
Average ($N = 24$) "Along Thread" SNAV Motion Detection Versus Intended Motion and ONAV Results

	Translation (mm)				Rotation (°)			
Intended motion	−5.00	−3.00	+3.00	+5.00	−4.92	−3.16	+3.16	+4.92
SNAV detection	−4.85	−2.89	+2.93	+4.94	−4.89	−3.18	+3.20	+4.91
ONAV detection	−4.77	−2.84	+2.88	+4.85	−4.89	−2.86	+3.13	+4.92

The average "along thread" motions detected for the phantom experiments are reported in Table 2. The SNAV answers for translation are in excellent agreement with the intended translations and are within the known ±0.2 mm accuracy of the motion phantom. The detected rotations are also within the known ±0.13° accuracy of the motion phantom for the sagittal rotations performed. The results yielded by the in-plane ONAV are also shown and agree well with both the SNAV results and the intended motion. Table 3 reports the maximum absolute motion detected along the other two axes where no motion occurred. ONAV detection is confounded by the through-plane rotation, and rotations of up to 0.7° were detected along the axes of no rotation. The SNAV never detected an off-axis rotation larger than 0.28° (some off-axis rotation may actually be occurring because of the difficulty of performing such small motions with a motion phantom). Detected off-axis translations were very small for both techniques (Table 3).

The SNAV and ONAV data were also acquired with an orientation such that the translations and rotations occurred on an axis that crossed the threads of the spherical helix SNAV trajectory. These "cross thread" results are presented in Tables 4 and 5. The average on-axis (Table 4) and maximum off-axis (Table 5) translation detection is as accurate as the "along thread" detection reported in Tables 2 and 3. As before, the ONAV results for translation and in-plane rotation match the intended motion well, but through-plane motion still confounds the off-axis rotation results. The rotations detected by the SNAV, however, do not match well with the intended rotation. We are currently investigating whether this is due to slight errors in the pulse sequence (i.e., the trajectories may not precisely form a spherical shell) or to other factors. The dense sampling results reported earlier show that all rotations were detected accurately, so the problem does not appear to be theoretical, but is more likely related to the implementation of the spherical helix trajectory. The strongest evidence that the helical SNAV is not perfectly tracing a path on the sphere was seen in the animations of SNAV data texture maps collected of the motion phantom at different rotated positions, which unfortunately is not readily appreciated on static images. For the "along thread" rotations, the animations looked as expected with stable features that rotate in a rigid body fashion. For the "cross thread" rotations, the features were sometimes observed to "warp." The most likely explanation for this observation is that the SNAV was leaving the spherical shell.

Table 6 reports an estimate of the precision of the SNAV technique based on the variability in results from the 24 repetitions of data collection at each phantom position. The SNAV is highly reproducible, with an average standard deviation along all axes of 0.007 mm and 0.017° for "along thread" detection and 0.01 mm and 0.03° for "cross thread" detection.

The magnitude registration and weighted least-squares inversion calculations were performed off-line with a combination of compiled code and MATLAB® (MathWorks Inc., Nattick, MA) scripts requiring several seconds total execution time on a desktop 750 MHz AMD Athlon PC. This amount of time would not be acceptable for real-time applications, but code optimization and implementation on an array processor would improve performance considerably.

DISCUSSION

The strategies presented so far for sampling a sphere are not the only possible strategies, and other schemes exist, with associated tradeoffs. Some of the preliminary sampling trajectories we implemented before settling on the double excitation equator-to-pole trajectory are presented in Fig. 8. Some of these trajectories use simpler equations (presented as Eqs. [13]–[17]) to trace a spherical helix starting at one pole and ending at the other.

$$\phi[n] = \frac{\pi n}{N} \quad [13]$$

$$\theta[n] = \frac{2\pi n T}{N} \quad [14]$$

$$k_x[n] = k_\rho \sin\phi[n]\cos\theta[n] \quad [15]$$

$$k_y[n] = k_\rho \sin\phi[n]\sin\theta[n] \quad [16]$$

$$k_z[n] = k_\rho \cos\phi[n] \quad [17]$$

Table 3
Average ($N = 24$) "Along Thread" SNAV and ONAV Detection Along Axes of No Intended Motion

	Translation (mm)				Rotation (°)			
Intended motion	−5.00	−3.00	+3.00	+5.00	−4.92	−3.16	+3.16	+4.92
SNAV detection	≤0.06	≤0.04	≤0.04	≤0.07	≤0.28	≤0.18	≤0.14	≤0.20
ONAV detection	≤0.05	≤0.03	≤0.02	≤0.05	≤0.35	≤0.35	≤0.35	≤0.70

Table 4
Average ($N = 24$) "Cross Thread" SNAV Motion Detection Versus Intended Motion and ONAV Results

	Translation (mm)				Rotation (°)			
Intended motion	−5.00	−3.00	+3.00	+5.00	−4.92	−3.16	+3.16	+4.92
SNAV detection	−4.95	−2.93	+2.94	+4.89	−5.52	−3.64	+3.44	+6.08
ONAV detection	−4.96	−2.93	+2.95	+4.91	−4.92	−3.16	+3.16	+5.24

The parameter T controls the number of threads or turns of the helix around the sphere. The three pole-to-pole trajectories using Eqs. [13]–[17] in Fig. 8a–c have fine sampling along the trajectory, but the sample spacing between threads of the helix is too large for accurate interpolation in the magnitude registration step of the SNAV algorithm. These early studies (26) with the single pole-to-pole trajectory (Fig. 8a) also revealed that it consistently underestimated z translations by ~10% or found a small z translation when none occurred. This is due to the linearity of the k_z trajectory, which in this case is not orthogonal to a possible phase ramp with time due to motion-induced effects. Multiple spirals collected in opposite directions can be interleaved (27) to overcome the k_z linearity problem and to provide finer sampling, as shown in Fig. 8b and c, but sampling is still more dense near the poles.

An alternative way to achieve better sample spacing and avoid high slew rates is to only sample a small patch or "ice cap" of the sphere's surface as shown in Fig. 8d, making it possible to use the more isotropic sample spacing yielded by Eqs. [9]–[11]. We are currently investigating such techniques based on sampling subsets of the sphere. Covering a smaller area of the sphere allows one to sample higher radii in k-space, which would be advantageous in situations where high spatial information is needed in the navigator data. For accurate motion detection the issues become engineering tradeoffs between the amount of spherical area sampled, the sampling density, the radius in k-space (i.e., feature detail, SNR, and phase wrapping complications), and maintaining trajectories that are mathematically orthogonal to linear-with-time motion-induced phase corruption.

The choice of k-space radius may also be tailored to optimize patient-specific results. One approach would be to acquire several "pilot" SNAV echoes at varying k-space radii in order to select an optimal radius based on features and SNR for each individual subject. Also, tracking structures that are deforming as well as moving as a rigid body may be possible by collecting SNAV data at a k-space radius that is not as strongly affected by the nonrigid deformations. For example, heart motion can be envisioned as consisting of an elastic component (myocardial contraction) as well as a roughly rigid body component (global motion due to diaphragmatic and chest wall excursion). It is conceivable that the rigid-body aspect of cardiac motion could be tracked with an SNAV that has a k_ρ properly sensitized to k-space features at the whole-organ level (i.e., low spatial frequencies).

For the motion phantom, the assumption that no material enters or leaves the imaging volume is certainly satisfied because of the finite extent of the phantom object. For in vivo applications, the full volume excitation and the coil sensitivity roll-off should minimize the effects of tissue signal at the boundaries of the FOV.

The SNAV approach has several theoretical advantages over multiplanar orthogonal ONAVs: it solves for all three rotational parameters and (separately) all three translational parameters simultaneously, it is sensitive to rotations about any axis, and there are no difficulties with "through-plane" rotations. For rigid-body motions the acquired k-space data never enters or leaves the sampled SNAV spherical shell if one assumes tissue does not enter or leave the FOV. Conversely, any rotation causes the k-space magnitude data to leave the plane for at least two of the three orthogonal ONAVs. The three ONAVs work independently; each determines rotation about its axis and provides no information to the others, limiting their effectiveness. By contrast, with an SNAV, all the sample points on the spherical surface participate in deducing the rotation about all three axes simultaneously.

The SNAV approach also has advantages over image registration techniques (8,9) for correcting time series data, such as in fMRI. The double excitation SNAV data is acquired as a snapshot in time (27 ms) vs. several seconds required to collect each stack of 2D images that form the 3D data sets used for image registration. Long data acquisition times invalidate the rigid-body motion assumption within a stack of 2D images that make up an individual image volume. For example in the Prospective Acquisition CorrEction (PACE) approach (9), each point in the time series consists of an image volume that is acquired as a series of 2D slices over a 2.5–4-s period of time. The probability that motion will occur during the period of time that a data volume is being acquired is quite high, making that dataset unsuitable for computation of rigid-body motion.

The angular spacing between adjacent points along a thread of the spherical helical sampling trajectory is ~5° at the equator, and the spacing between threads is ~4°. However, the effective resolution of an SNAV for detecting

Table 5
Average ($N = 24$) "Cross Thread" SNAV and ONAV Detection Along Axes of No Intended Motion

	Translation (mm)				Rotation (°)			
Intended motion	−5.00	−3.00	+3.00	+5.00	−4.92	−3.16	+3.16	+4.92
SNAV detection	≤0.12	≤0.05	≤0.05	≤0.07	≤0.32	≤0.18	≤0.04	≤0.03
ONAV detection	≤0.06	≤0.03	≤0.03	≤0.06	≤0.35	≤0.00	≤0.70	≤1.19

Table 6
SNAV Reproducibility ($N = 24$), Average Standard Deviation for All Axes

	Translation (mm)	Rotation (°)
Along thread	0.007	0.017
Cross thread	0.010	0.030

rotations is far better than this, since essentially all the points are participating to some extent. The resolution may be estimated as follows. Given points uniformly distributed about a spherical surface, and a rotation about an arbitrary axis, points farthest from this axis are the most important in precisely determining the rotation angle, and points near the poles of this axis are of little value. However, spherical geometry is such that "most" points are always far away from any axis and thus are useful: the average perpendicular distance of points to an arbitrary axis is $(\pi/4)k_\rho$ or $\sim 0.79k_\rho$. If this distance is considered to be the "effectiveness factor" of a given point, 2000 uniform points have an effective resolution of 0.23° about any axis (or rather, *about all axes simultaneously*). Uniform spherical sampling is thus an efficient way to arrange points so that most will be sensitive to any possible rotation.

In conclusion, determining rigid-body 3D rotations and translations accurately with SNAVs is feasible with a small enough number of points to be practically acquired in tens of milliseconds. Accurate rotational and translational motion measurements about all three axes, suitable for retrospective or prospective motion correction in a clinical setting, can be obtained with this technique. The SNAV technique could be used prospectively to correct global rigid-body motion in image-to-image motion in fMRI or to partially correct global motion effects in cardiac imaging. Interview motion in scans with long TR times could also be corrected with such motion detection.

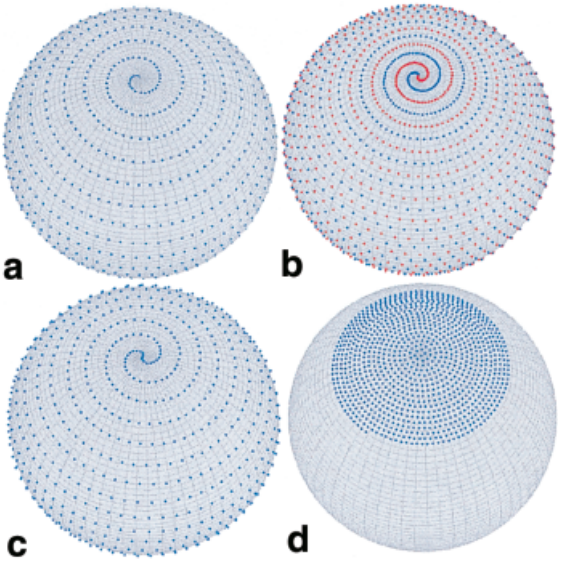

FIG. 8. **a:** Alternate sphere sampling strategies using lower slew rate trajectories. Using Eqs. [13]–[17] with $N = 1008$ and $T = 17$ it is possible to satisfy slew rate limits at $k_\rho = 0.396$ cm^{-1} ($9.5\Delta k$). However, this sampling is denser at the poles of the sphere, with large distances between the threads of the helix. **b:** An interleaved helix in a subsequent TR improves the sampling density. **c:** Without using a second TR, a pole-to-pole-to-pole trajectory can be used, but the high slew rate requirement reduces the number of turns of the helix. **d:** Finally using Eqs. [9]–[11] with $N = 8094$, the first 1008 points sample a patch or "ice cap" covering approximately one-eighth the total area of the sphere.

ACKNOWLEDGMENTS

The authors thank the members of the Mayo MRI research lab for their valuable contributions to this work.

REFERENCES

1. Runge VM, Clanton JA, Partain CL, James Jr AK. Respiratory gating in magnetic resonance imaging at 0.5 T. Radiology 1984;151:521–523.
2. Bailes DR, Gilderdale DJ, Bydder GM, Collins AG, Firim DN. Respiratory ordered phase encoding (ROPE): a method for reducing respiratory motion artifacts in MR imaging. J Comput Assist Tomogr 1985;9:835–838.
3. Korin HW, Riederer SJ, Bampton AEH, Ehman RL. Altered phase-encoding order for reduced sensitivity to motion in three-dimensional MR imaging. J Magn Reson Imaging 1992;2:687–693.
4. Jhooti P, Wiesmann F, Taylor AM, Gatehouse PD, Yang GZ, Keegan J, Pennell DJ, Firmin DN. Hybrid ordered phase encoding (HOPE): an improved approach for respiratory artifact reduction. J Magn Reson Imaging 1998;8:968–980.
5. Korin HW, Felmlee JP, Riederer SJ, Ehman RL. Spatial-frequency-tuned markers and adaptive correction for rotational motion. Magn Reson Med 1995;33:663–669.
6. Haase A, Frahm J, Matthaei D, Hanicke W, Merboldt K. FLASH imaging: rapid NMR imaging using low flip-angle pulses. J Magn Reson 1986;67:258–266.
7. Oppelt A, Graumann R, Barfuss H, Fischer H, Hartl W, Shajor W. FISP—a new fast MRI sequence. Electromedia 1986;54:15–18.
8. Maas L, Frederick B, Renshaw P. Decoupled automated rotational and translational registration for functional MRI time series data: the DART registration algorithm. Magn Reson Med 1997;37:131–139.
9. Thesen S, Heid O, Mueller E, Schad LR. Prospective acquisition correction for head motion with image-based tracking for real-time MRI. Magn Reson Med 2000;44:457–465.
10. Glover GH, Pauly JM. Projection reconstruction techniques for reduction of motion effects in MRI. Magn Reson Med 1992;28:275–289.
11. Glover GH, Lee AT. Motion artifacts in fMRI: comparison of 2DFT with PR and spiral scan methods. Magn Reson Med 1995;33:624–635.
12. Shankaranarayanan A, Wendt M, Lewin JS, Duerk JL. Two-step navigatorless correction algorithm for radial k-space MRI acquisitions. Magn Reson Med 2001;45:277–288.
13. Pipe JG. Motion correction with PROPELLER MRI: application to head motion and free-breathing cardiac imaging. Magn Reson Med 1999;42:963–969.
14. Ehman RL, Felmlee JP. Adaptive technique for high-definition MR imaging of moving structures. Radiology 1989;173:255–263.
15. Wang Y, Rossman PJ, Grimm RC, Riederer SJ, Ehman RL. Navigator-echo-based real-time respiratory gating and triggering for reduction of respiration effects in three-dimensional coronary MR angiography. Radiology 1996;198:55–60.
16. Fu ZW, Wang Y, Grimm RC, Rossman PJ, Felmlee JP, Riederer SJ, Ehman RL. Orbital navigator echoes for motion measurements in magnetic resonance imaging. Magn Reson Med 1995;34:746–753.
17. Lee CC, Jack CR, Grimm RC, Rossman PJ, Felmlee JP, Ehman RL, Riederer SJ. Real-time adaptive motion correction in functional MRI. Magn Reson Med 1996;36:436–444.
18. Lee CC, Grimm RC, Manduca A, Felmlee JP, Ehman RL, Riederer SJ, Jack CR. A prospective approach to correct for inter-image head rotation in fMRI. Magn Reson Med 1998;39:234–243.
19. Ward HA, Riederer SJ, Grimm RC, Ehman RL, Felmlee JP, Jack CR. Prospective multiaxial motion correction for fMRI. Magn Reson Med 2000;43:459–469.
20. Grimm RC, Riederer SJ, Ehman RL. Real-time rotation correction using orbital navigator echoes. In: Proceedings of the 5th Annual Meeting of ISMRM, Vancouver, Canada, 1997. p 1899.

21. Press WH, Teukolsky, Vetterling WT, Flannery BP. Numerical recipes in C, 2nd ed. New York, NY: Cambridge University Press; 1992.
22. Wong STS, Roos MS. A strategy for sampling on a sphere applied to 3D selective RF pulse design. Magn Reson Med 1994;32:778–784.
23. Hajnal JV, Myers R, Oatridge A, Schwieso JE, Young IR, Bydders GM. Artefacts due to stimulus correlated motion in functional imaging of the brain. Magn Reson Med 1994;31:283–291.
24. Friston KJ, Williams SR, Howard R, Frackowiak RSJ, Turner R. Movement-related effects in fMRI time-series. Magn Reson Med 1996;35: 346–355.
25. Lee CC, Ward HA, Sharbrough FW, Meyer FB, Marsh WR, Raffel C, So EL, Cascino GD, Shin C, Yu Y, Riederer SJ, Jack CR. Assessment of functional MR imaging in neurosurgical planning. Am J Neuroradiol 1999;20:1511–1519.
26. Welch EB, Manduca A, Grimm RC, Ward HA, Jack CR. Spherical navigator echoes for full 3D rigid body motion measurement in MRI. In: Proceedings of SPIE Med Imaging 2001;3322:796–803.
27. Welch EB, Manduca A, Grimm RC, Ward HA, Jack CR. Spherical navigator echoes for 3D rigid body motion detection. In: Proceedings of the 9th Annual Meeting of ISMRM, Glasgow, Scotland, 2001. p 291.